Reynolds Number Effects on Wing Shock Buffet Unsteadiness

Luke Masini* and Sebastian Timme[†]
University of Liverpool, Liverpool, L69 3GH, United Kingdom

Andrew J. Peace[‡]
Aircraft Research Association Ltd., Bedford, MK41 7PF, United Kingdom

The flow physics governing transonic shock-buffet onset remain disputed with their elucidation typically limited to model-scale wind-tunnel and numerical data. This paper addresses the inherent dynamics at buffet onset by complementing high-quality experimental data with scale-resolving simulation. Delayed detached-eddy simulations of a large civil aircraft wing are analysed, both at model scale to reproduce the experimental flow data (Reynolds number of 3.75 million) and at full scale to assess the influence of Reynolds number at flight conditions (27 million). The simulations are interrogated against experimental dynamic pressure-sensitive paint data, providing critical insight into the flow. Modal analysis techniques including proper orthogonal decomposition and dynamic mode decomposition are applied, revealing outboard-running waves along the shock confined to the tip region, similar to previously reported buffet cells believed to constitute the shock-buffet instability, in addition to an inboard-running low-frequency behaviour exclusive to the experimental data. The full-scale simulation highlights lower lift fluctuations owing to a further downstream shock oscillation over a smaller chordwise distance and a more limited spanwise extent, when compared to a model-scale simulation at the same angle of attack, indicating a slightly delayed buffet-onset incidence at full scale. The flow physics are similar in both cases, characterised by spanwise outboard pressure propagation in the wing-tip region at a Strouhal number of about 0.22, based on mean aerodynamic chord and reference freestream velocity. These findings further the understanding of edge-of-the-envelope flow physics and clarify scaling effects on shock buffet on a real-world configuration, ultimately informing future wing design and buffet-control strategies.

Nomenclature

C_L	=	lift coefficient
c_p	=	pressure coefficient
f	=	frequency, Hz
m	=	number of snapshots
n	=	number of computational mesh points
Re_{MAC}	=	Reynolds number based on mean aerodynamic chord (MAC)
St	=	Strouhal number based on chord for aerofoils or mean aerodynamic chord for wings
t	=	physical time, s
y^+	=	nondimensional wall distance
α	=	angle of attack, deg.
Δ_0	=	mesh target spacing, m
$\Lambda_{1/4}$	=	quarter-chord sweep angle, deg.
Λ_{LE}	=	leading-edge sweep angle, deg.
μ_t/μ	=	ratio of turbulent viscosity μ_t to dynamic viscosity μ

*PhD Student, School of Engineering, l.masini@liverpool.ac.uk, AIAA Student Member.

[†]Senior Lecturer, School of Engineering, sebastian.timme@liverpool.ac.uk, AIAA Member.

[‡]Chief Scientist, apeace@ara.co.uk, AIAA Member.

I. Introduction

Transonic shock buffet on civil aircraft wings remains a key challenge for aerodynamicists, with no unequivocal explanation to the flow mechanism governing its onset despite over half a century of research [1]. At critical combinations of Mach number and angle of attack, shock-wave/boundary-layer interaction (SWBLI) on the wing's upper surface induces intermittent boundary-layer separation and self-sustained shock oscillation. This aerodynamic instability, typically termed as *shock buffet*, generates unsteady loads and a consequent structural response, referred to as buffeting, mutually interacting with the flow. In effect, passenger comfort, the aircraft's performance, handling qualities, and structural fatigue life are degraded. Moreover, certification requirements stipulate a cruise design point free from any buffeting, such that buffet onset limits the flight envelope at high Mach number and load factor, motivating continuous scrutiny from both industry and academia.

Extensive research on this reportedly aerodynamic instability has elucidated distinct characteristics on nominally two-dimensional aerofoils and swept three-dimensional wings. In the case of two-dimensional buffet on aerofoils, periodic shock oscillations have been reported in several experimental [2–4] and numerical studies [5–9]. These oscillations are characterised by narrow-band spectral peaks at low frequencies—at least an order of magnitude lower than those associated with turbulence in the incoming boundary layer. Large shock excursions of around 20% chord length have been reported between Strouhal numbers of 0.05 and 0.08, based on chord length [10]. Two theories have been put forward along the years to explain the self-sustained shock oscillations. The first model, commonly referred to as Lee's model [11], relies on an acoustic feedback loop whereby acoustic waves from the shock and the trailing edge sustain the shock oscillations. The second model proposed by Crouch *et al.* [12] and further supported by Sartor *et al.* [13] explains aerofoil shock buffet as a Hopf bifurcation with a globally unstable mode of the flow appearing above critical conditions. Whilst there are similarities between these two models, such as the frequency of the shock oscillations and the propagation of pressure waves within the boundary layer together with radiation of acoustic waves from the trailing edge, a unified aerofoil shock buffet model consolidating these observations is yet to be proposed. Several numerical techniques have been employed to simulate two-dimensional shock buffet, including unsteady Reynolds-averaged Navier–Stokes (RANS) simulations [5, 7, 8], detached-eddy simulations (DES), including the zonal [6] and the delayed (DDES) approach [9], and large-eddy simulations (LES) [14, 15]. Most of these studies consider a fully turbulent boundary layer upstream of the SWBLI. However, recent work considering laminar flow conditions, where laminar-to-turbulent transition takes place in the region of the SWBLI, has reported shock excursions confined to the shock foot over smaller chordwise distances and at frequencies of over an order of magnitude higher than the fully turbulent case [16, 17]. Furthermore, complex interaction between the shock wave, pressure waves and the boundary layer have been reported from direct numerical simulation at moderate Reynolds number [18].

The flow physics governing swept-wing shock buffet remain unclear, not least because of limited research specifically on transport-type wings and the far more complex three-dimensional interactions involved [19]. It is generally agreed that wing buffet differs from the two-dimensional case in two main aspects. First, a narrow frequency peak no longer characterises the phenomenon. Instead, swept-wing shock buffet has a broadband higher-frequency signature at Strouhal numbers between 0.2 and 0.6, based on mean aerodynamic chord (MAC). Second, shock oscillation takes place over shorter chordwise distances which can vary along the span depending on the extent of the separation region downstream of the shock. These particular characteristics which highlight different physical mechanisms governing aerofoils or infinite straight wings and swept wings were observed from early flight test data [20] and wind-tunnel tests [21–23]. More recent experimental tests [24–26] employing highly-instrumented wind-tunnel models have confirmed the broadband signature and have further elucidated the phenomenon by computing characteristic convection speeds. The advent of novel optical techniques such as dynamic pressure-sensitive paint (DPSP), essentially a fast-response pressure-sensitive paint (PSP) coupled with high-frame-rate image capturing, has greatly progressed the understanding of the complex shock motion that takes place at edge-of-the-envelope conditions. Although early applications in transonic wind tunnels [27, 28] had limited resolution or coverage, more recent experiments [26, 29] have acquired unsteady pressure over the entire wing surface enabling detailed analysis of the shock dynamics.

This improved understanding has been complemented by numerical studies. Notably, a systematic study employing time-marching unsteady RANS simulations [30] revealed contrasting characteristics between straight and low sweep angle wings, and wings with a sweep angle above 20°. At low sweep angles, shock oscillation is chordwise dominated and similar to that on aerofoils. On moderately and highly swept wings, a spanwise propagation of pressure along the shock and pockets of shock-induced separation, coined therein as buffet cells, were observed moving outboard. A similar numerical approach on infinite swept wings has shown similar characteristics between buffet cells linked with transonic shock buffet and low-speed stall cells [31] and a biglobal stability analysis [32] has identified spatial modes with outboard propagation that become unsteady with the introduction of sweep. Increasingly sophisticated

simulations including scale-resolving DES have been conducted on several geometries [33–35] demonstrating the capability of capturing complex shock motion and characteristic spanwise propagation of pressure and buffet cells. The flow conditions simulated in these studies are well-beyond buffet onset and do not discuss the flow physics in the vicinity of onset. The latter aspect has been recently studied with a triglobal stability analysis on a finite wing [36], linking buffet cells to an unstable linear eigenmode, and another delayed DES study [37] which identified a pulsating separated region periodically perturbing the shock.

In this paper, we address the inherent dynamics governing onset both at wind-tunnel and full scale. This is of great interest to industry since understanding the effect of flight conditions is critical to allow meaningful interpretation of sub-scale wind-tunnel test data and its relation to the full-scale flight vehicle. We combine high-quality experimental data captured in [26] and further analysed in [38, 39] with scale-resolving DES. This work forms part of a larger effort initiated under the European Union Clean Sky Buffet Control of Transonic Wings (BUCOLIC) project, that included the acquisition of an extensive buffet-focussed DPSP experimental database [26] and delayed DES [35]. Further analysis of the experimental dataset [38, 39] has identified two distinct phenomena in shock-buffet conditions—a low-frequency shock unsteadiness for Strouhal numbers between 0.05 and 0.15 along the whole span, predominantly propagating pressure inboard, and a broadband higher-frequency behaviour for Strouhal numbers between 0.2 and 0.5, confined to the wing-tip region propagating pressure outboard towards the tip. This outboard behaviour was captured by DES [35, 37] and is similar to previously reported buffet cells, believed to constitute the shock-buffet instability on conventional swept wings. These massive datasets are analysed with data-based modal identification techniques which are rather attractive recently to extract and characterise the pertinent flow features [37, 38, 40, 41]. Herein, we extend the DES and analysis techniques in [37] to study the influence of flight Reynolds number and full-scale geometry on shock-buffet onset. This work contributes to the ongoing discussion and renewed interest in edge-of-the-envelope flow physics, ultimately informing future wing design and routes to buffet control.

This paper is organised as follows. The wing geometry and flow conditions together with the numerical approach using the DLR-TAU software package and an overview of the post-processing techniques are outlined in Sec. II. Section III analyses the main results from steady-state and time-marching simulations and provides qualitative and quantitative comparisons with experimental data, giving confidence in the numerical approach and the full-scale influence on the inherent dynamics of shock buffet. The main conclusions are finally discussed in Sec. IV.

II. Methodology

A. Geometry and Flow Conditions

The test case is a half wing-body configuration called RBC12, which represents a commercial aircraft of a typical 1970s/1980s design. The wing is twisted and tapered, with an aspect ratio of 7.78, a constant quarter-chord sweep angle $\Lambda_{1/4}$ of 25° and a leading-edge sweep angle Λ_{LE} of 28.3°. When scaled down to wind-tunnel dimensions by a factor of 17.5, the model has a semi-span of 1.104 m and the MAC is 0.279 m. For numerical simulation, transition was fixed at model scale to replicate the wind-tunnel test with boundary-layer tripping, whereas fully-turbulent conditions were considered at full scale. With regards to transition locations on the upper surface, these are at 10% local chord at the wing tip, 14% at the crank and 15% at the root, whilst this is at 5% on the lower surface. The fuselage was tripped 0.104 m aft of the nose. Far-field conditions using a hemispherical domain are applied at a distance of 25 semi-span lengths (around 90 MACs) and a symmetry boundary condition is imposed on the centre plane.

The model-scale simulation aims to reproduce the experimental aerodynamic flow field at buffet onset conditions. The geometry is considered rigid excluding any static deformation such that the study focusses exclusively on the inherent fluid dynamics of shock buffet. The RBC12 model has been extensively tested in the Aircraft Research Association Transonic Wind Tunnel and any static deformation is believed to have negligible influence, as discussed in [26]. At the design Mach number of 0.80, a critical angle of attack of around 3.0° has been obtained from unsteady RANS simulations [42] and a global stability analysis [43] when using the Spalart-Allmaras (S-A) model for turbulence closure. In the present simulations, the angle of attack was set at 3.1° after running a number of exploratory time-marching simulations. In order to simulate the influence of flight conditions and Reynolds number effects on buffet onset, atmospheric conditions at an altitude of 38 000 ft based on the U.S. Standard Atmosphere [44] were considered. The flow conditions for both simulations are summarised in Table 1.

Table 1   Flow conditions for scale-resolving simulations at model scale and full scale.

Parameter	Model scale	Full scale
Mach number	0.80	0.80
Angle of attack, deg.	3.1	3.1
Reference temperature, K	266.5	216.7
Reference pressure, kPa	66.0	20.7
Reference length, m	0.279	4.881
Air density, kg/m^3	0.863	0.333
Re_{MAC}, million	3.75	27.03

B. Numerical Approach

1. Flow Solver and Numerical Settings

Both steady-state and time-accurate simulations were performed using the unstructured finite-volume solver TAU, developed by the German Aerospace Center (DLR) and widely used in the European aerospace sector. The turbulence model of choice was the negative S-A model [45]. The second-order central scheme was used to discretise the inviscid fluxes of the mean flow equations in all simulations. However, whilst scalar dissipation was used for steady RANS simulations, minimal fourth-order matrix-valued artificial dissipation was combined with a second-order energy conserving skew-symmetric convection operator to minimise discretisation errors in DDES and provide stabilisation [46]. Different schemes were also chosen regarding the convective fluxes of the turbulence model—the first-order Roe scheme was employed for RANS while the second-order central scheme was used for the DDES. Previous experience has shown that the prediction of unsteady regions is sensitive to the choice of turbulence-model discretisation due to eddy viscosity levels, which can inhibit the unsteadiness [35, 47]. Gradients of the flow variables were reconstructed with a least squares approach which minimises errors in a hybrid mesh, such as those used herein.

The original DES formulation [48], motivated by the challenges imposed by massively separated flows at high Reynolds number, with pure LES not yet feasible due to its sheer computational cost, is designed to treat entire boundary layers with a RANS model and apply LES in separated-flow regions. However, this formulation is highly-dependent on grid spacing and can exhibit incorrect behaviour in thick boundary layers and shallow separation regions. Delayed DES [49] was developed to shield the boundary layer from LES treatment which would lower the eddy viscosity below the RANS level, otherwise leading to depleted Reynolds stresses and lower skin friction, ultimately causing premature grid-induced separation. This newer formulation helps to satisfy the original aim of DES by maintaining the RANS function in thick boundary layers while allowing the LES function after massive separation [50]. Herein, we employ DDES with low-Reynolds-number correction, readily available in TAU and previously used on the RBC12 well-beyond shock-buffet onset [35]. Switching between RANS and LES regions is controlled by a filter based on maximum edge spacing. Numerical parameters are blended between these regions via the hybrid low-dissipation low-dispersion scheme (LD2) [51], which provides a numerical weighting function to discriminate between well-resolved vortex-dominated flow regions, treated with the LD2 scheme [52, 53], and coarser-grid regions, treated with the more dissipative and dispersive reference scheme. Low dissipation is ensured by setting the inverse fourth-order dissipation coefficient to 256 for the reference scheme and 1024 for the resolved region.

In the scale-resolving time-marching simulations, the standard second-order dual-time stepping approach was used for temporal discretisation. The physical time-steps are 1 μs and 20 μs at model scale and full scale, respectively. These correspond to a CFL number of $O(1)$, calculated using the grid spacing in the focus region and a conservative measure of 1.5 times freestream velocity [54]. A dynamic Cauchy convergence criterion was applied for dual-time iterations, controlled by the drag coefficient with a relative error smaller than 10^{-8} within the last 20 iterations. Moreover, a minimum of 100 inner iterations was always performed such that the density residual converges to at least an order of magnitude. For the full-scale simulation, a minimum of 150 inner iterations was set instead.

Table 2   Mesh information both at model scale and full scale.

Parameter	Model scale	Full scale
n, million	50.4	52.2
Elements, million	203.1	207.0
First cell height, m	5.30×10^{-7}	1.35×10^{-6}
Δ_0, m	0.0007	0.0150
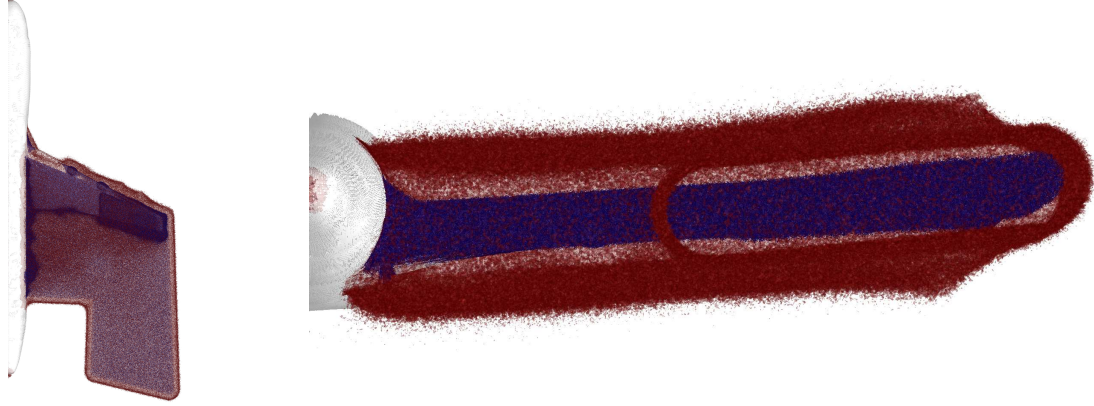
Fig. 1   Mesh isovolumes highlighting refinement by LES mesh sources. Highly-refined elements are shaded in blue, larger elements are shaded in red.

2. Computational Mesh

Hybrid meshes were produced using the SOLAR mesh generator [55] generally following industry best-practice guidelines [56]. Rather than just scaling the model-scale mesh, a new mesh was generated after scaling the geometry in order to maintain the same y^+ of around 0.5, such that wall functions are not used. The meshes consist of hexahedral-, prism- and tetrahedral-type elements and were highly refined to resolve the turbulent structures in the separated zone. Some key figures of the meshes are summarised in Table 2.

Two large mesh sources for the LES focus region were added to the standard sources routinely used in complex wing geometries, as depicted in Fig. 1. The first source extends from 60% semi-span to just outboard of the wing tip in a spanwise sense, and from just aft of the leading edge to around 4 MACs downstream of the trailing edge reaching the tail, in the chordwise direction. In this region, the surface elements have a target spacing of $\Delta_0 \approx 0.003$ MAC, $\Delta_0 = max(\Delta_x, \Delta_y, \Delta_z)$. This is the finest region in the mesh and was informed by experimental analysis [26, 38] and previous simulations [35, 43], both showing separation on this wing to occur first on outboard sections. The second source covers the inboard region, extending from the wing root to 60% semi-span, and approximately 2 MACs downstream of the crank. While elements in this region have $\Delta_0 \approx 0.007$ MAC, this source was primarily included to have a smooth transition from the highly refined outboard region, in the case that any turbulent eddies propagate inboard.

3. Data Outputs and Post-Processing

The scale-resolving simulations were started from partially converged RANS solutions at an angle of attack of 3.1°. An initial transient results as high eddy-viscosity regions arising from the steady RANS simulations are destroyed after which the flow develops self-sustained unsteadiness. The model-scale simulation was run for a total physical time of 0.121 s (121 000 timesteps) and is considered as a complete simulation with eighteen buffet cycles allowing statistical analysis. The total physical time of the full-scale simulation is 1.19 s (59 500 timesteps). Flow-field data was gathered at every 250 time steps, equating to a sampling frequency of 4 kHz at model scale and 0.2 kHz at full scale, respectively. Surface data was output at 10 kHz and 0.2 kHz. These sampling rates were chosen to resolve the dynamics of swept-wing buffet, namely, large-scale shock motion and associated buffet cells in the separated region. Moreover,

both qualitative and quantitative comparisons with the BUCOLIC experimental dataset are possible, including direct comparison with the unsteady surface pressure data measured with DPSP.

In addition to traditional post-processing including pressure distribution and Fourier analysis, these massive datasets are analysed using modal analysis techniques. These include proper orthogonal decomposition (POD) and dynamic mode decomposition (DMD) and are essentially purely data-driven algorithms. The flow-field data is decomposed into a set of spatio-temporal modes aiding the elucidation of the flow dynamics. POD gives a set of spatially-orthogonal modes which capture the most energetic structures in the data, ranked by the contribution in optimising the variance of the data. In contrast, DMD identifies spatial modes with a characteristic frequency and a growth/decay rate, determined from the DMD eigenvalues. An extensive overview of modal analysis techniques applied to fluid flows has been published [40]. Herein, these techniques are applied to both experimental and numerical datasets. The *method of snapshots* [57] is used giving a much smaller eigenvalue problem of size $m \times m$ rather than $n \times n$. Modal decomposition is performed using the parallelised `modred` library [58] developed for this task, employing a vector-space approach which eliminates the need to store all the snapshots in memory. This enables the modes to be computed from the whole dataset.

III. Results and Analysis

A. Steady-State Simulations

Steady-state simulations were performed on the generated meshes, and analysed, before running any time-accurate simulations. The angle of attack was varied incrementally by 0.1° while the convergence of the density residual norm was closely monitored as a possible indicator of physically unsteady flow. Good convergence of at least nine orders of magnitude was obtained up to 2.8° at both model and full scale. At angles of attack higher than 2.9°, the density residual levels out and does not converge beyond five orders of magnitude at model scale. At full scale, the residual converges to six orders of magnitude up to 3.0° and does not converge beyond five orders of magnitude at higher angles of attack. Those stagnating convergence norms suggest unsteady flow.

Figure 2 presents a comparison between experimental and numerical data based on the surface pressure coefficient. Time-averaged data from DPSP is shown in Figs. 2a–2d whereas Figs. 2e–2l depict the steady-state pressure distributions at four angles of attack of both model and full scale. It should be noted that the experimental data without a flow angle correction results in a lower lift coefficient for a specific angle of attack, as shown later in Fig. 7. However, changes to the surface-flow phenomena are similar with increments in angle of attack from below to beyond shock-buffet onset. Notably, trailing-edge separation confined to the outboard wing rapidly merges with the shock-induced separation bubble resulting in a region of localised separation on the outboard wing. Focussing on the RANS simulations, skin friction lines are included to aid the flow visualisation whilst the boundaries of reversed-flow regions (based on streamwise velocity component) are shown by the dashed lines. At 2.6°, the RANS simulations predict a shock-induced separation bubble which extends from mid-span and almost reaches the wing tip. At model scale, trailing-edge separation occurs between 70 and 89% semi-span. Although this is not visible at full scale, as soon as the angle of attack is slightly increased to 2.7°, the incipient separation at the trailing edge starts to merge with the shock-induced separation and the reverse-flow region widens with angle of attack. This corroborates the flow physics around buffet onset analysed at a wide range of Mach numbers experimentally [38, 39] and numerically [59] on the RBC12. This localised separated flow perturbs the shock causing an upstream motion of the shock position with angle of attack, sometimes referred to as inverse shock motion, eventually generating spanwise oscillations visible from the shock trace at 3.1°. These observations indicate that separated flow at full scale is only slightly delayed compared to model scale, and therefore, the shock buffet onset incidence is expected to be similar to that at model scale. This is investigated by time-marching unsteady simulations and discussed in more detail in Sec. III.B.1.

In order to quantitatively assess the steady-state RANS simulations, Fig. 3 shows a comparison between RANS results at model scale and experimental pressure-tap data, for the two spanwise stations indicated in Fig. 2. These pressure distributions clarify the formation of a separation region on the outboard wing and an associated upstream shock movement with increasing angle of attack. The 3.1° pressure distribution from RANS clearly depicts the shock-induced separation and pressure divergence close to the trailing edge due to incipient separation. Experimentally, while suction levels continue to increase in the supersonic region with angle of attack, pressure levels downstream of the shock are not constant between $\alpha = 2.9°$ and 3.3° indicating separated flow. In fully-turbulent flight conditions, the shock sits further downstream as a result of a thinner boundary layer at high Reynolds number. This is highlighted in Fig. 4 which compares the pressure distributions from the RANS simulations at 73% semi-span.
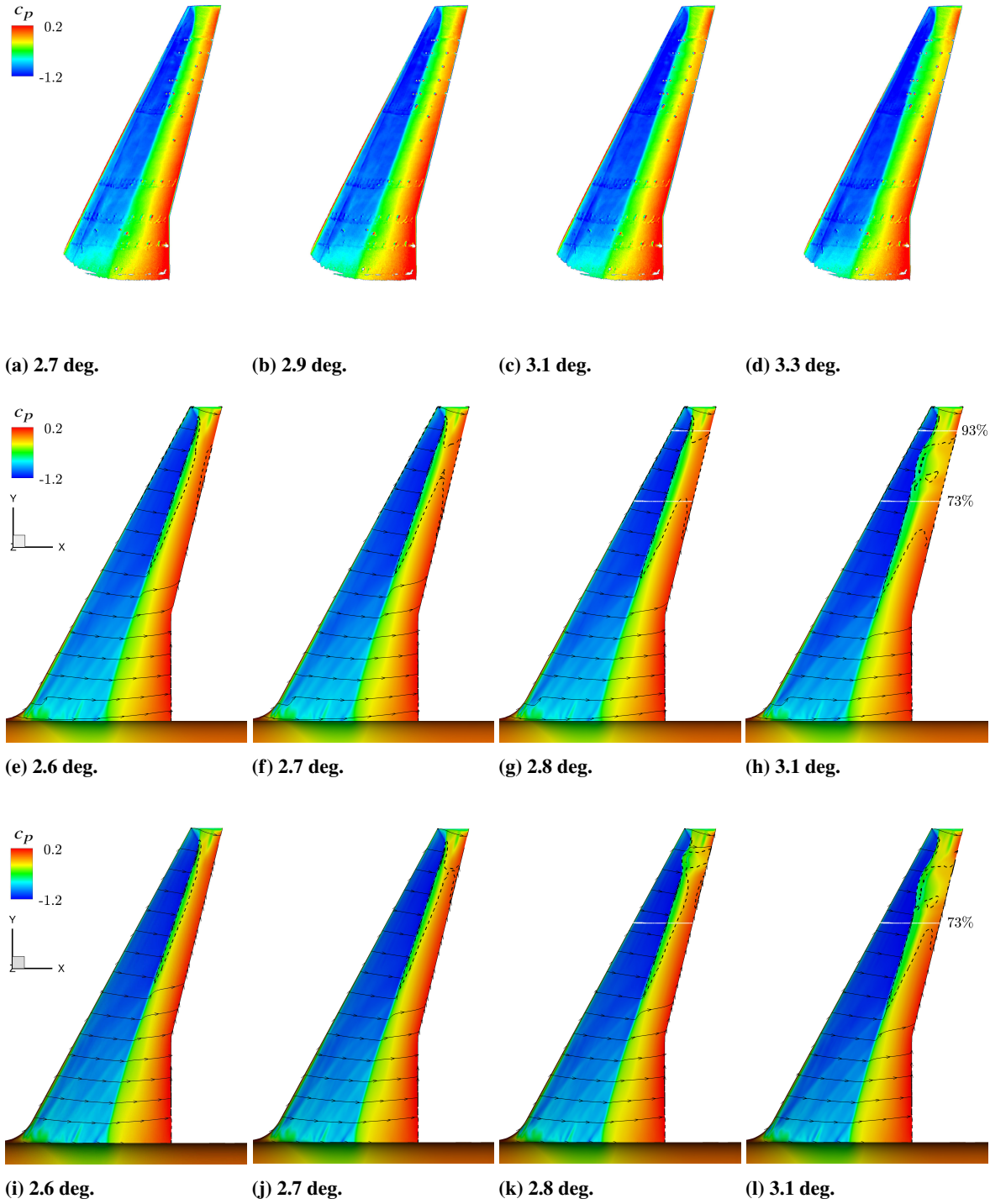
(a) 2.7 deg.   **(b) 2.9 deg.**   **(c) 3.1 deg.**   **(d) 3.3 deg.**

(e) 2.6 deg.   **(f) 2.7 deg.**   **(g) 2.8 deg.**   **(h) 3.1 deg.**

(i) 2.6 deg.   **(j) 2.7 deg.**   **(k) 2.8 deg.**   **(l) 3.1 deg.**

Fig. 2   **Comparison of surface pressure coefficient distribution from experiment and steady-state simulations at a number of angles of attack; (a–d) mean surface pressure from experimental DPSP, (e–h) model-scale simulations and (i–l) full-scale simulations. The surface flow is highlighted by skin friction lines and boundaries of reverse-flow regions are denoted by the dashed lines.**

(a) 73% semi-span
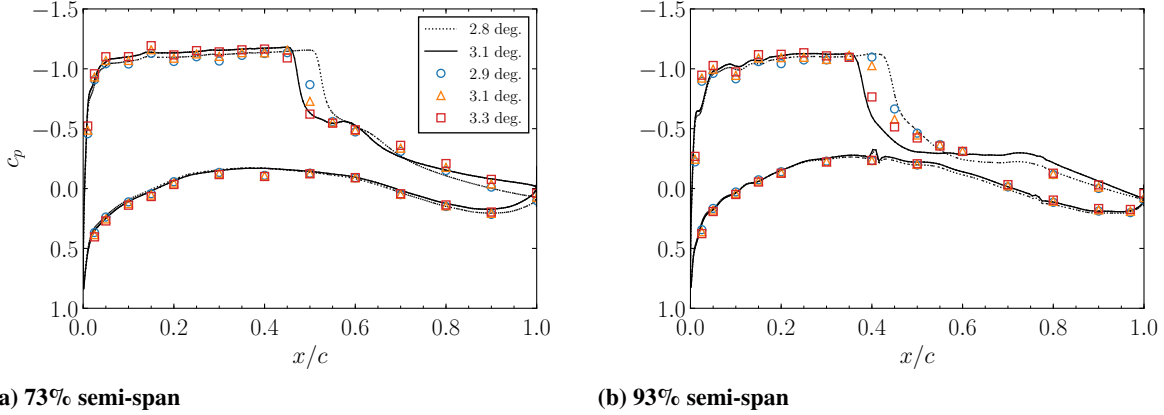
(b) 93% semi-span

Fig. 3 Chordwise pressure distributions from steady-state simulations at model scale and experimental static pressure taps at two outboard sections.
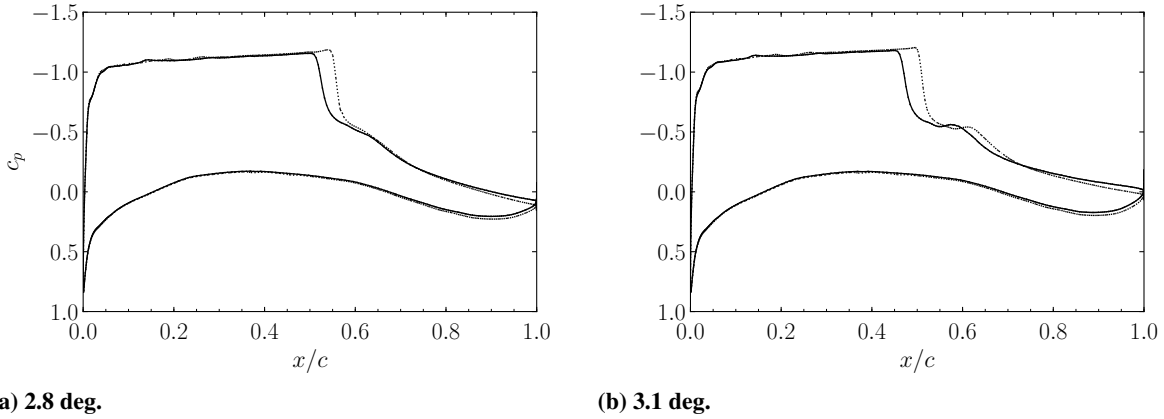

(a) 2.8 deg.

(b) 3.1 deg.

Fig. 4 Comparison of chordwise pressure distributions at 73% semi-span; solid lines depict model scale, dotted lines represent full scale.

B. Delayed Detached-Eddy Simulations

1. Development of Self-Sustained Flow Unsteadiness

The development of flow unsteadiness was assessed by monitoring the time histories of integrated values such as the lift and drag coefficients. Figure 5 shows the lift coefficient history at different angles of attack in the vicinity of buffet onset of scale-resolving simulations performed both at model scale and full scale. At model scale, the 3.1° simulation was pursued since the flow unsteadiness at 2.9° was expected to decay. Previous studies have shown that numerically, the critical angle of attack is 3.0° as explained in Section II.A. At full scale, the time-accurate simulations were performed starting from 2.9° based on the indication of physically unsteady flow from the steady-state simulations. However, self-sustained lift fluctuations due to shock buffet were only observed at 3.1°. Focussing on the time histories at 3.1°, it is clear that after an initial transient where large-scale shock motion causes large fluctuations, more periodic oscillations take place. This part of the signal ($t > 0.0305$ s at model scale, $t > 0.18$ s at full scale) has been considered as developed shock buffet and is used for the signal processing and subsequent analysis. The model-scale simulation is characterised by periodic lift fluctuations caused by an oscillating shock perturbed by a pulsating separation bubble [37]. At full scale, lift fluctuations are smaller in magnitude and show disturbances with regards to periodicity.

The frequency content of the lift fluctuations was studied by computing power spectral density (PSD) data using Burg's method [60]. This autoregressive model was selected since it can provide high frequency resolution even for short signals, typical for such expensive simulations. PSD data presented in Fig. 6 was computed using a single window and an order of 4000 at model scale and 2000 at full scale. These parameters were chosen after a parametric study and a
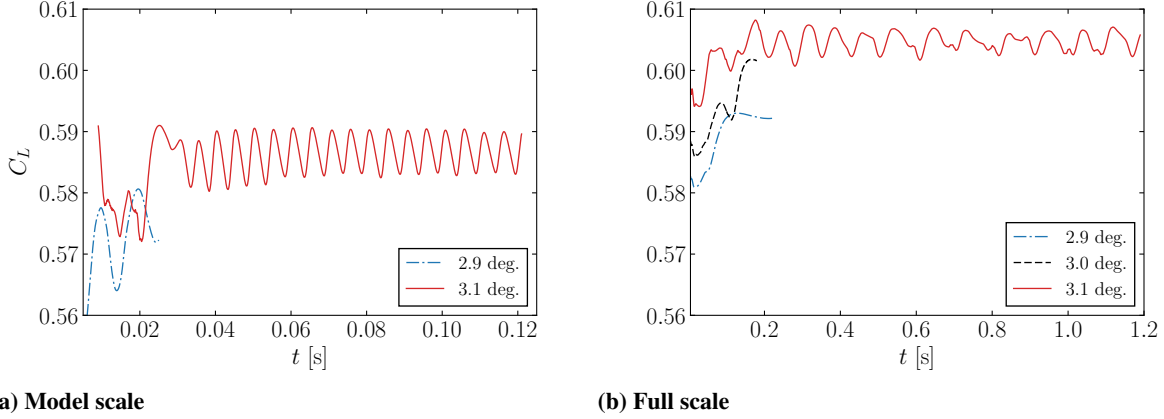
8

(a) Model scale

(b) Full scale

Fig. 5   Time history of the lift coefficient as obtained by DDES (note different time axes).
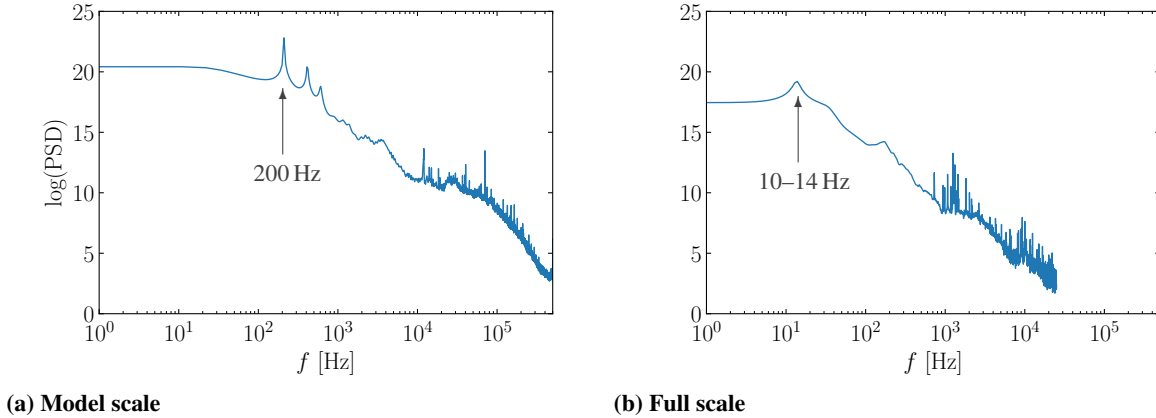

(a) Model scale

(b) Full scale

Fig. 6   Power spectral density of lift fluctuations from DDES.

smaller order was used at full scale since the signal length is approximately half that at model scale. The frequency spectrum at model scale is characterised by a clear peak at 200 Hz ($St = 0.22$) and its harmonics. At full scale, the peaks are less well defined due to the lower number of buffet cycles that have been simulated and less periodic nature of the fluctuations, however, a bump is clearly visible between 10 and 14 Hz ($St = 0.21$ to 0.29). These frequencies are compatible with typical values reported for swept-wing shock buffet [20, 23, 24].

Numerical and experimental data of the lift coefficient variation with angle of attack is provided in Fig. 7. Experimental data was measured with a five-component strain-gauge balance and two sets of data are shown in the figure. Points denoted by filled circles have been corrected for interference effects including wall constraint and paint effect in the case of incidence and wind-tunnel blockage for Mach number. Since the flow may also experience a small flow angle in the vicinity of a wind-tunnel model, an estimated flow angle correction of 0.35° was applied, represented by the open circles. An estimate has to be used since direct measurement of the flow angle is restricted on half-models mounted to the wind-tunnel floor. This estimate is based on several other tests comparing half-models and sting-mounted full models in the same wind tunnel. Numerical data from both steady-state and scale-resolving simulations are presented, and for the latter, the time-averaged value is depicted by the squares together with minimum and maximum fluctuations in time, denoted by the vertical lines. At model scale, good correlation was obtained between numerical and experimental data, which includes the flow angle estimation, giving confidence in the numerical simulations. DDES data from the current simulation at 3.1° and a previous simulation at 3.8° [35] are included. At 3.1°, lift fluctuations of approximately ±0.05 around the mean value resulted due to periodic shock oscillations on the outboard wing, as highlighted in Sec. III.B.2. Numerical simulation at full scale results in higher C_L values in accordance with the pressure distributions presented in Figs. 2i–2l and 4. The fluctuations around the time-averaged value in the DDES at 3.1° are smaller at approximately ±0.03, owing to smaller shock excursions when compared to the model-scale simulation.
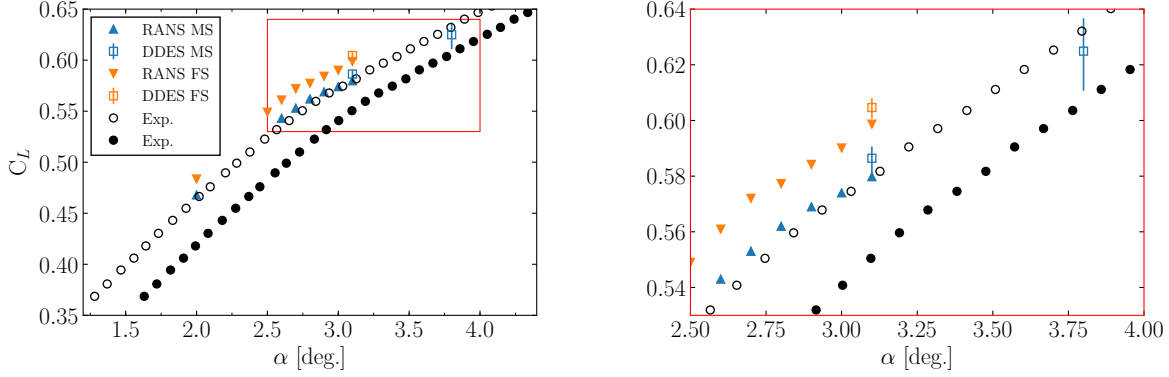
9

Fig. 7 Lift coefficient with angle of attack from experiment (open circles include flow angle correction and filled circles exclude it) and CFD (vertical line denotes minimum and maximum of time fluctuations). MS and FS denote model scale and full scale, respectively.
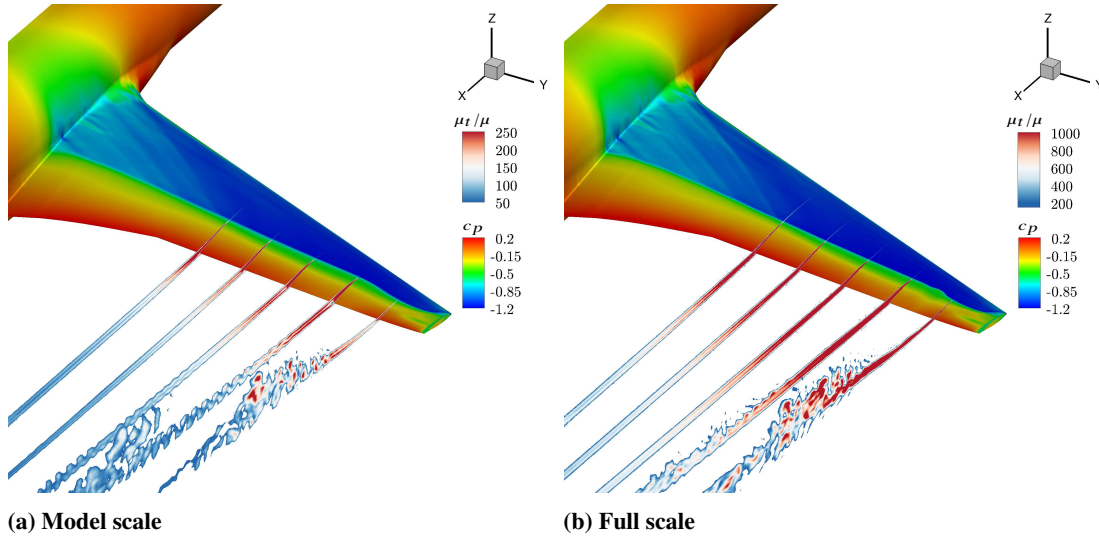

(a) Model scale

(b) Full scale

Fig. 8 Surface pressure coefficient distribution and slices of eddy-viscosity ratio at instantaneous time steps corresponding to a high lift coefficient value. Note different scaling in eddy-viscosity ratio.

Figure 8 shows instantaneous surface pressure distributions and slices of eddy-viscosity ratio, μ_t/μ, the ratio of turbulent viscosity to laminar viscosity. The snapshots correspond to instances with a peak C_L value at which the shock is sitting downstream of its mean position. The slices are between 50% and 90% semi-span in steps of 10%. The highly-refined region encapsulating the outboard wing allows for LES treatment and resolved turbulent content is depicted in the outboard slices. The percentage of grid points treated in LES mode was approximately 61% and 59% at model scale and full scale, respectively. These values exhibit slight variations in time due to instantaneous fluctuations in the delay switch function in the DDES formulation and intermittent flow separation. During a shock-buffet cycle, shock-induced separation takes place during the upstream phase of the shock oscillation (corresponding to troughs in the C_L time history). At the instances shown in Fig. 8, there is no flow separation over the wing and detached eddies have propagated downstream in the wake. A comparison of the eddy-viscosity ratio from the model- and full-scale simulations reveals higher values in the latter, implying less resolved content. This is expected primarily due to two factors. First, the Reynolds number is higher by approximately a factor of 7—higher Reynolds number means that the ratio of largest to smallest turbulent length scales increases [61]. Second, the reference length, and accordingly the average cell size, is increased by a factor of 17.5. Hence, more of the turbulent length scales are modelled, rather than resolved for the full-scale simulation. In both simulations, the mesh refinement allows for large regions with resolved turbulence and the eddy-viscosity ratio is much lower than unsteady RANS simulations on the same wing [35].

10

(a) DPSP (3.3 deg.) mode 1   (b) Model-scale DDES $(0.021 \leq t \leq 0.121\,\text{s})$ (c) Model-scale DDES $(0.0305 \leq t \leq 0.121\,\text{s})$ (d) Full-scale DDES $(0.18 \leq t \leq 1.19\,\text{s})$
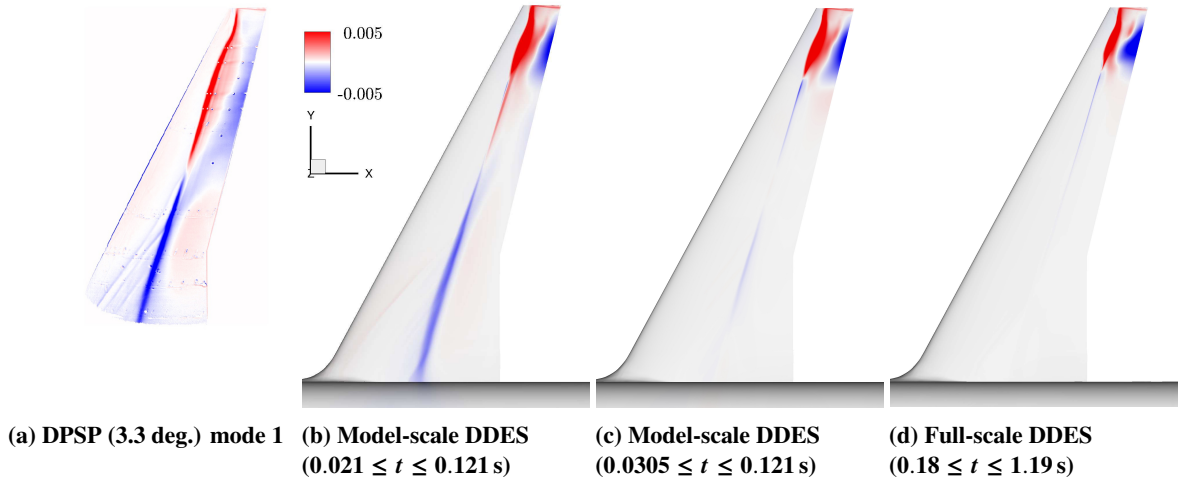
Fig. 9   Spatial component of dominant POD mode from DPSP, model- and full-scale DDES surface pressure coefficient data, coloured by spatial amplitudes.

(a) DPSP (3.3 deg.) mode 8   (b) Model-scale DDES $(0.021 \leq t \leq 0.121\,\text{s})$ (c) Model-scale DDES $(0.0305 \leq t \leq 0.121\,\text{s})$ (d) Full-scale DDES $(0.18 \leq t \leq 1.19\,\text{s})$
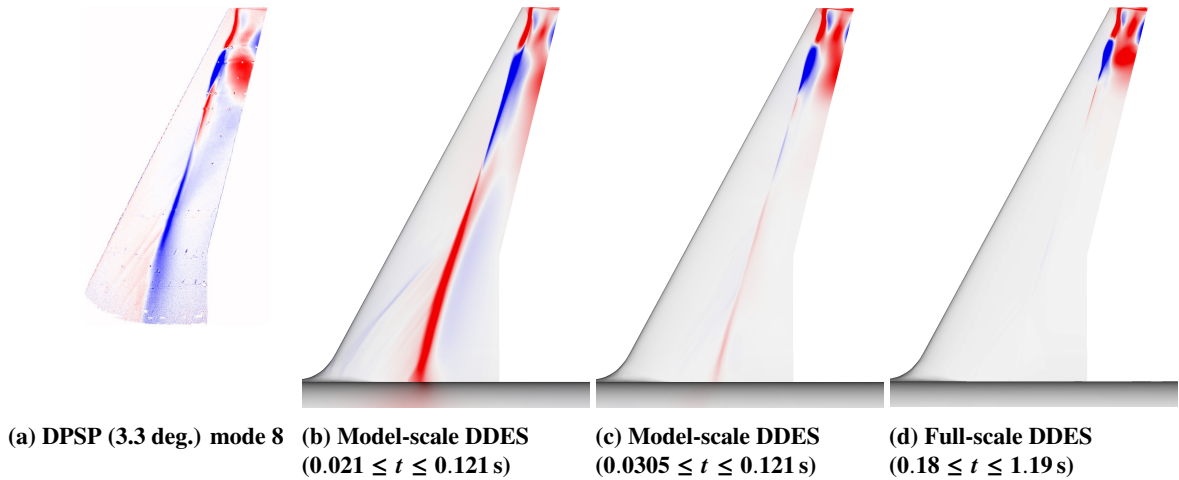
Fig. 10   Spatial component of a less dominant POD mode from DPSP, model- and full-scale DDES surface pressure coefficient data. The spatial amplitudes are coloured as in Fig. 9.

2. Modal Analysis

Modal analysis techniques including POD and DMD were applied to the unsteady datasets to provide a spatio-temporal representation of the dominant flow dynamics. A direct comparison of modes obtained from an analysis of experimental DPSP surface pressure snapshots and those from numerical simulation is presented next.

The dominant flow features corresponding to the largest fluctuations in surface pressure were extracted by a POD analysis. Figure 9 depicts the spatial component of dominant POD modes from both experimental and numerical data. In all cases, the greatest contribution is along the shock unsteadiness and the region downstream of the shock. Experimentally, an unsteady shock was observed along the whole span, with coexisting inboard-running propagation at around 70 Hz ($St \approx 0.07$) and outboard-running perturbations at higher frequency (>200 Hz, $St > 0.22$), confined to the outboard wing [38, 39]. In the model-scale DDES, large-scale shock motion along the whole span takes place in the transient phase, initially propagating pressure towards the root, reminiscent of the wind-tunnel observations. This is associated with the low-frequency fluctuations in lift coefficient depicted in Fig. 5a. Flow unsteadiness in the inboard region decays after a few cycles and the periodic fluctuations that follow are generated by localised patches of separated flow on the outer wing. It is worth noting that similar results were obtained from a numerical time-linearised
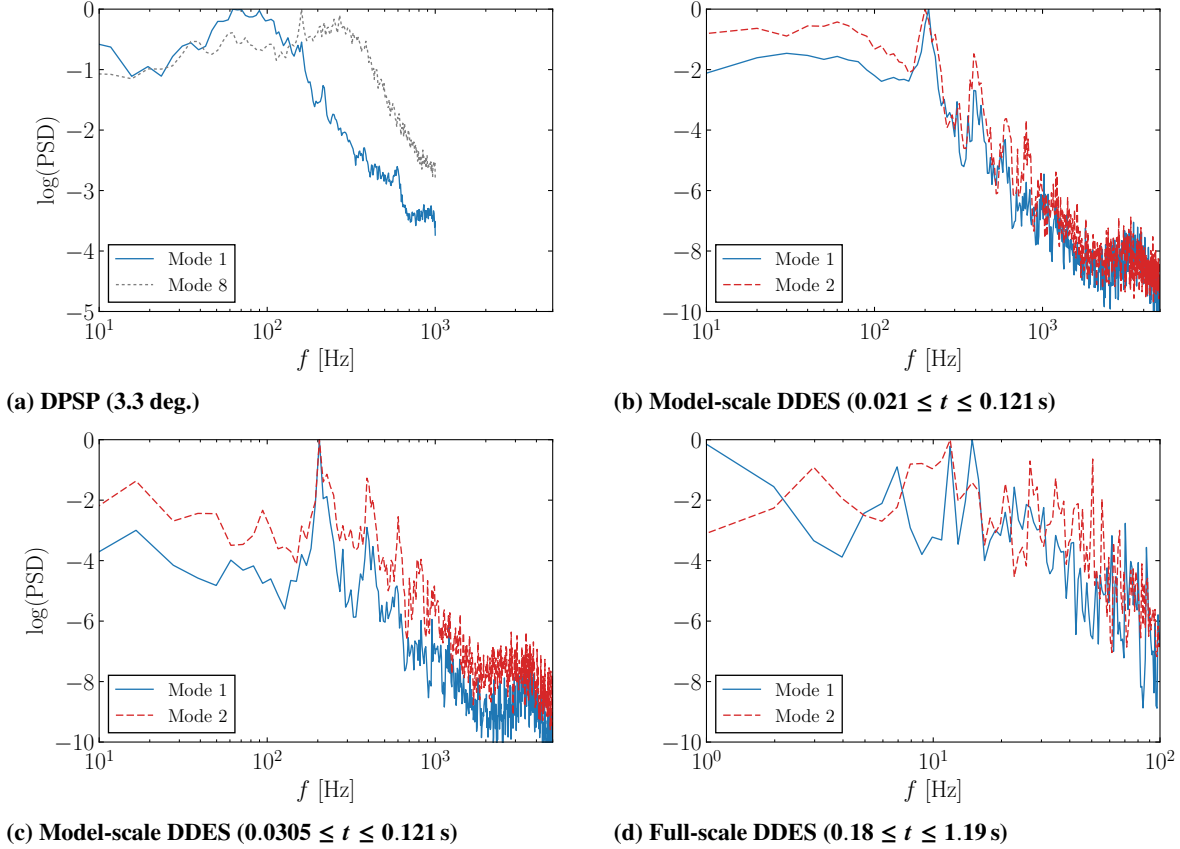
11

(a) DPSP (3.3 deg.)

(b) Model-scale DDES (0.021 ≤ t ≤ 0.121 s)

(c) Model-scale DDES (0.0305 ≤ t ≤ 0.121 s)

(d) Full-scale DDES (0.18 ≤ t ≤ 1.19 s)

Fig. 11 **Power spectral density data of POD temporal coefficients for selected modes. Note different frequency axis for full-scale simulation.**

analysis [43], whereby forced wing vibration excites a low-frequency response and distinct higher-frequency peaks at typical swept-wing buffet frequencies. A slight increment in the angle of attack amplifies the higher-frequency peak greatly, while the low-frequency peak exhibits lower sensitivity. This lower-frequency behaviour seems to be dominated by the shock unsteadiness but questions remain whether this is a purely aerodynamic global instability which imposes its own dynamics, or whether it is a noise-amplifier problem having a convective nature.

For these reasons, the POD analysis was repeated on two sets of snapshots in the case of the model-scale simulation—the first including a part of the transient phase (0.021 ≤ t ≤ 0.121 s) and the second consisting only of the periodic oscillations (0.0305 ≤ t ≤ 0.121 s). In Fig. 9, there is greater similarity between the dominant mode from DPSP (Fig. 9a) and the model-scale DDES including a low-frequency cycle (Fig. 9b) because of the shock curvature along the span and inboard unsteadiness. The spatial amplitudes represent positive or negative perturbations around the mean pressure value, depending on their sign and the corresponding temporal coefficient. To illustrate, at a positive temporal coefficient, regions of higher and lower pressure are depicted by positive (red) and negative (blue) spatial amplitudes. Therefore, the shock sits upstream of its mean position on the outboard wing inducing flow separation. Further inboard, the shock is downstream and the flow remains attached. Since the inboard unsteadiness decays, Fig. 9c is dominated by the outboard unsteadiness showing similar dynamics over this region. The dominant POD mode, obtained at full scale in Fig. 9d, similarly shows the largest contribution on the outboard wing. The shock oscillates over smaller chordwise distances and emanates from slightly further outboard than at model scale. This corroborates the smaller fluctuations in lift coefficient previously shown in Fig. 7.

Another example of a resulting POD mode is depicted in Fig. 10 from which similar observations can be made. Experimentally, a number of modes are related to the structural response of the model and mode 8 is shown in Fig.10a—the first one, ranked by POD energy, to capture the shock rippling on outboard sections and causing pockets of shock-induced separation that follow the upstream shock excursions. In the case of the DDES, the spatial components
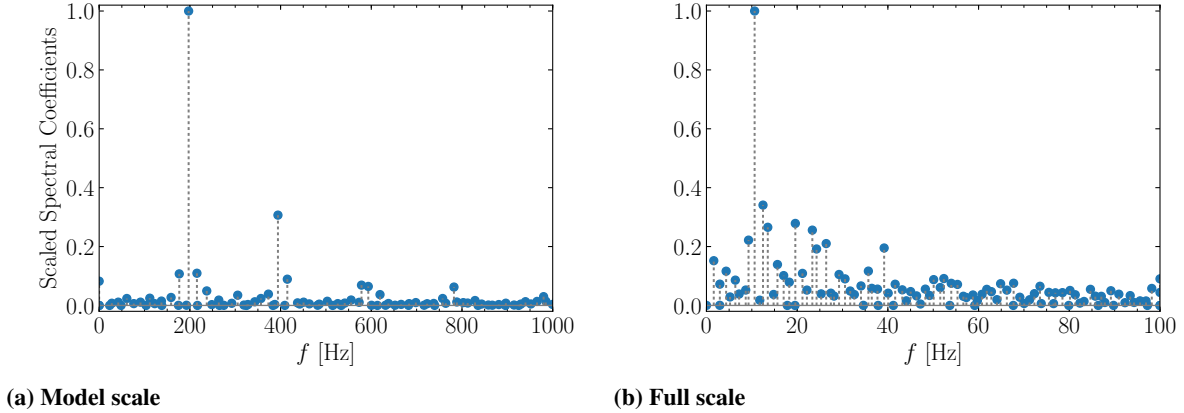
(a) Model scale

(b) Full scale

Fig. 12 **DMD spectrum for surface pressure snapshots from model- and full-scale DDES.**

of mode 2 are shown. To obtain the temporal behaviour of these modes, PSD data based of the temporal coefficients corresponding to the modes presented in Figs. 9 and 10 are shown in Fig. 11. Considering the DPSP dataset, mode 1 is centred at lower frequencies around 70 Hz, typical of the low-frequency shock unsteadiness, whereas mode 8 shifts to a higher frequency above 200 Hz that is characteristic of the shock-buffet instability. With regards to the model-scale DDES, modes 1 and 2 have a clear peak at 200 Hz, matching the primary peak obtained from the lift fluctuations in Fig. 6a. PSD levels for the set that includes a part of the transient are higher at low frequencies below 100 Hz corresponding to the shock rippling along the span and the inboard unsteadiness. Focussing on the full-scale simulation, the frequency spectrum is less defined due to a shorter time signal. However, peaks are visible at 11 and 14 Hz, within the range of the spectral bump of the PSD of lift coefficient fluctuations in Fig. 6b. The PSD data for the numerical signal was computed using Burg's method [60] whilst Welch's method [62] was used for the longer DPSP signal. In all cases, the PSD data was normalised by the maximum value.

A dynamic mode decomposition of the surface pressure data was conducted to isolate flow phenomena based on frequency and identify dynamically-important modes. Mode sorting was based on the spectral coefficients computed from the norm of the first projection coefficient. To take into account the time evolution of each DMD mode, the spectral coefficients were scaled by the absolute value of the corresponding eigenvalue to promote growing and slowly-decaying modes, while reducing the peaks of modes with large norms but of a quickly-decaying nature [63]. The computed DMD spectrum based on surface pressure snapshots from the model- and full-scale simulations is shown in Fig. 12. The spectral coefficients, excluding that of the mean flow mode, were normalised by the maximum value. At model scale, the dominant DMD mode has a frequency of 197 Hz ($St = 0.22$), while this is 11 Hz ($St = 0.23$) at full scale, closely matching the respective frequency of lift fluctuations. These modes are depicted in Figs. 13 and 14, respectively. It is evident that the spatial structures of dominant DMD modes are very similar to POD modes 1 and 2, presented previously in Figs. 9 and 10. The complex-valued spatial fields from DMD have the advantage of clarifying the dynamics at a single frequency. Variations between the real and imaginary parts provide information regarding the pressure propagations. The magnitude of the complex number highlights the intensity of pressure perturbations while the phase variation indicates the direction of propagation. A comparison of the magnitude of the dominant DMD modes in Figs. 13c and 14c immediately elucidates pressure perturbations that are confined closer to the wing tip and a smaller shock oscillation at full scale. The shock dynamics are similar in both simulations with the phase angle gradually decreasing in the spanwise direction along the shock, corresponding to pressure propagation in the outboard direction. A phase difference of approximately π between the shock foot and the trailing edge corroborates the flow physics implied by the opposite signs of the POD spatial amplitudes in these regions, i.e. trailing-edge separation occurs when the shock is upstream of its mean position. Apparent discontinuities in the phase angle are due to phase wrapping and have no physical meaning.

IV. Conclusions

In the transonic flow around a large aircraft wing geometry, two phenomena have previously been identified experimentally—a lower-frequency shock unsteadiness with a wavelength almost extending along the entire span and a higher-frequency cellular pattern with a more localised spanwise extent of about a local chord, typically referred to
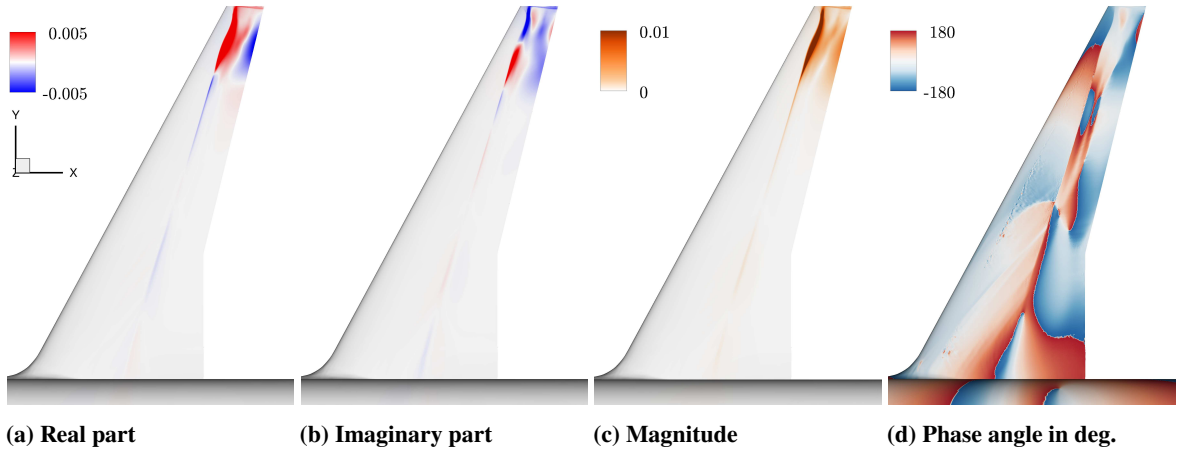
(a) Real part   **(b) Imaginary part**   **(c) Magnitude**   **(d) Phase angle in deg.**

Fig. 13   Dominant DMD mode from the model-scale DDES (0.0305 ≤ t ≤ 0.121 s) having a frequency of 197 Hz.

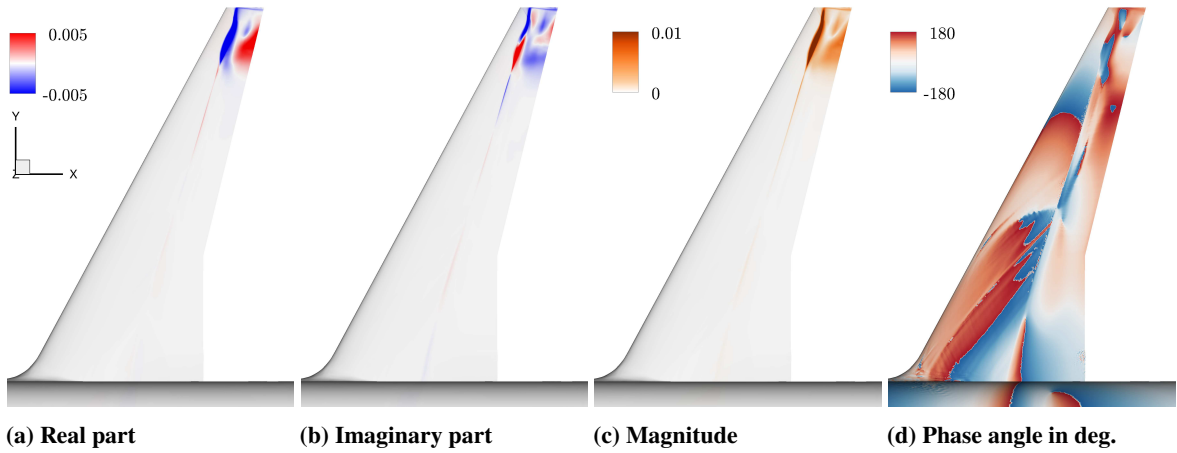**(a) Real part**   **(b) Imaginary part**   **(c) Magnitude**   **(d) Phase angle in deg.**

Fig. 14   Dominant DMD mode from the full-scale DDES (0.18 ≤ t ≤ 1.19 s) having a frequency of 11 Hz.

as shock buffet, which is the focus of this work. A synergistic study complementing a unique experimental dynamic pressure-sensitive paint dataset and delayed detached-eddy simulation has been presented to clarify whether flight Reynolds number has a substantial influence on shock-buffet onset and its governing flow physics.

For the wing studied, time-marching scale-resolving simulations at wind-tunnel and full scale indicate that shock-buffet onset is only slightly delayed at flight conditions and confirm similar inherent dynamics. In both cases, patches of localised separated flow periodically perturb the shock wave, and vice versa, via a self-sustaining mechanism. The model-scale simulation was directly compared with the experimental dataset using two data-based modal identification techniques applied to surface pressure snapshots. This was motivated by their ability to extract and characterise the pertinent flow features from vast data volumes. Dominant modes from proper orthogonal decomposition and dynamic mode decomposition have spatial structures with the greatest contribution on the outboard shock and its separated region downstream. Shock oscillation confined to the wing-tip region results in spanwise pressure propagation in the outboard direction. These perturbations have a Strouhal number of approximately 0.22, based on mean aerodynamic chord, corresponding to the same spectral signature of the lift fluctuations. At higher Reynolds number, the magnitude of lift fluctuations is smaller as a further downstream shock oscillates over shorter chordwise distances and a more limited spanwise extent. Modes identified from dynamic pressure-sensitive paint data highlight a similar behaviour characterised by outboard pressure propagation along the shock in the same frequency range that characterises swept-wing shock buffet. However, the lower-frequency shock unsteadiness behaviour is unique to the wind-tunnel test and does not feature in the fully developed buffet phase of the fluid-only numerical simulations.

This study has addressed the inherent dynamics in the vicinity of buffet onset bridging a gap in shock-buffet literature which mostly focuses on conditions well beyond onset. Qualitative and quantitative comparison with experimental data gives confidence in the numerical approach motivating this study of scaling effects on shock buffet on a real-world configuration, ultimately allowing meaningful interpretation of sub-scale experimental and numerical data and how it relates to the full-scale flight vehicle. The finding that the shock-buffet dynamics are inherently the same in an industrial-size transonic tunnel and at flight scale accentuates that wind-tunnel testing remains an integral part of current and future research on the buffet phenomenon, including its delay.

Acknowledgements

References

[1] Hilton, W. F., and Fowler, R. G., "Photographs of Shock Wave Movement," Tech. Rep. NPL R&M No. 2692, National Physical Laboratory, 1947.

[2] McDevitt, J. B., and Okuno, A. F., "Static and Dynamic Pressure Measurements on a NACA 0012 Airfoil in the Ames High Reynolds Number Facility," Tech. Rep. NASA TP 2485, Jun. 1985.

[3] Jacquin, L., Molton, P., Deck, S., Maury, B., and Soulevant, D., "Experimental Study of Shock Oscillation over a Transonic Supercritical Profile," *AIAA Journal*, Vol. 47, No. 9, 2009, pp. 1985–1994.

[4] Feldhusen-Hoffmann, A., Statnikov, V., Klaas, M., and Schröder, W., "Investigation of Shock–Acoustic-Wave Interaction in Transonic Flow," *Experiments in Fluids*, Vol. 59, No. 15, 2018, pp. 1–13.

[5] Brunet, V., "Computational Study of Buffet Phenomenon with Unsteady RANS Equations," 2003. AIAA 2003-2679.

[6] Deck, S., "Numerical Simulation of Transonic Buffet over a Supercritical Airfoil," *AIAA Journal*, Vol. 43, No. 7, 2005, pp. 1556–1566.

[7] Xiao, Q., Tsai, H.-M., and Liu, F., "Numerical Study of Transonic Buffet on a Supercritical Airfoil," *AIAA Journal*, Vol. 44, No. 3, 2006, pp. 620–628.

[8] Iovnovich, M., and Raveh, D. E., "Reynolds-Averaged Navier-Stokes Study of the Shock-Buffet Instability Mechanism," *AIAA Journal*, Vol. 50, No. 4, 2012, pp. 880–890.

[9] Grossi, F., Braza, M., and Hoarau, Y., "Prediction of Transonic Buffet by Delayed Detached-Eddy Simulation," *AIAA Journal*, Vol. 52, No. 10, 2014, pp. 2300–2312.

[10] Lee, B. H. K., "Self-Sustained Shock Oscillations on Airfoils at Transonic Speeds," *Progress in Aerospace Sciences*, Vol. 37, No. 2, 2001, pp. 147–196.

[11] Lee, B. H. K., "Oscillatory Shock Motion Caused by Transonic Shock Boundary-Layer Interaction," *AIAA Journal*, Vol. 28, No. 5, 1990, pp. 942–944.

[12] Crouch, J., Garbaruk, A., Magidov, D., and Travin, A., "Origin of Transonic Buffet on Aerofoils," *Journal of Fluid Mechanics*, Vol. 628, 2009, pp. 357–369.

[13] Sartor, F., Mettot, C., and Sipp, D., "Stability, Receptivity, and Sensitivity Analyses of Buffeting Transonic Flow over a Profile," *AIAA Journal*, Vol. 53, No. 7, 2014, pp. 1980–1993.

[14] Garnier, E., and Deck, S., "Large-Eddy Simulation of Transonic Buffet over a Supercritical Airfoil," *Turbulence and Interactions: Proceedings the TI 2009 Conference*, edited by M. Deville, T.-H. Lê, and P. Sagaut, Springer Berlin Heidelberg, Berlin, Heidelberg, 2010, pp. 135–141. doi:10.1007/978-3-642-14139-3_16.

[15] Fukushima, Y., and Kawai, S., "Wall-modeled Large-Eddy Simulation of Transonic Buffet over a Supercritical Airfoil at high Reynolds Number," 2017. AIAA 2017-0495.

[16] Brion, V., Dandois, J., Abart, J.-C., and Paillart, P., "Experimental Analysis of the Shock Dynamics on a Transonic Laminar Airfoil," *Progress in Flight Physics*, Vol. 9, 2017, pp. 365–386.

[17] Dandois, J., Mary, I., and Brion, V., "Large-Eddy Simulation of Laminar Transonic Buffet," *Journal of Fluid Mechanics*, Vol. 850, 2018, pp. 156–178.

[18] Zauner, M., De Tullio, N., and Sandham, N. D., "Direct Numerical Simulations of Transonic Flow Around an Airfoil at Moderate Reynolds Numbers," *AIAA Journal*, Vol. 57, No. 2, 2019, pp. 597–607.

[19] Giannelis, N., Vio, G., and Levinski, O., "A Review of Recent Developments in the Understanding of Transonic Shock Buffet," *Progress in Aerospace Sciences*, Vol. 92, 2017, pp. 39–84.

[20] Hwang, C., and Pi, W. S., "Northrop F-5 A Aircraft Transonic Buffet Pressure Data Acquisition and Response Analysis," *Journal of Aircraft*, Vol. 12, No. 9, 1975, pp. 714–720.

[21] Riddle, D., "Wind-Tunnel Investigation of Surface-Pressure Fluctuations Associated with Aircraft Buffet," 1975. AIAA 1975-0067.

[22] Roos, F., "The Buffeting Pressure Field of a High-Aspect-Ratio Swept Wing," 1985. AIAA 1985-1609.

[23] Benoit, B., and Legrain, I., "Buffeting Prediction for Transport Aircraft Applications Based on Unsteady Pressure Measurements," 1987. AIAA 1987-2356.

[24] Dandois, J., "Experimental Study of Transonic Buffet Phenomenon on a 3D Swept Wing," *Physics of Fluids*, Vol. 28, No. 016101, 2016, pp. 1–17.

[25] Koike, S., Ueno, M., Nakakita, K., and Hashimoto, A., "Unsteady Pressure Measurement of Transonic Buffet on NASA Common Research Model," 2016. AIAA 2016-4044.

[26] Lawson, S., Greenwell, D., and Quinn, M. K., "Characterisation of Buffet on a Civil Aircraft Wing," 2016. AIAA 2016-1309.

[27] Steimle, P. C., Karhoff, D.-C., and Schröder, W., "Unsteady Transonic Flow over a Transport-Type Swept Wing," *AIAA Journal*, Vol. 50, No. 2, 2012, pp. 399–415.

[28] Merienne, M.-C., Le Sant, Y., Lebrun, F., Deleglise, B., and Sonnet, D., "Transonic Buffeting Investigation Using Unsteady Pressure-Sensitive Paint in a Large Wind Tunnel," 2013. AIAA 2013-1136.

[29] Sugioka, Y., Koike, S., Nakakita, K., Numata, D., Nonomura, T., and Asai, K., "Experimental Analysis of Transonic Buffet on a 3D Swept Wing Using Fast-Response Pressure-Sensitive Paint," *Experiments in Fluids*, Vol. 59, No. 108, 2018, pp. 1–20.

[30] Iovnovich, M., and Raveh, D. E., "Numerical Study of Shock Buffet on Three-Dimensional Wings," *AIAA Journal*, Vol. 53, No. 2, 2015, pp. 449–463.

[31] Plante, F., Dandois, J., and Laurendeau, E., "Similitude Between 3D Cellular Patterns in Transonic Buffet and Subsonic Stall," 2019. AIAA 2019-0030.

[32] Crouch, J. D., Garbaruk, A., and Strelets, M., "Global Instability Analysis of Unswept- and Swept-Wing Transonic Buffet Onset," 2018. AIAA 2018-3229.

[33] Brunet, V., and Deck, S., "Zonal-Detached Eddy Simulation of Transonic Buffet on a Civil Aircraft Type Configuration," 2008. AIAA 2008-4152.

[34] Ishida, T., Hashimoto, A., Ohmichi, Y., Aoyama, T., and Takekawa, K., "Transonic Buffet Simulation over NASA-CRM by Unsteady-FaSTAR Code," 2017. AIAA 2017-0494.

[35] Sartor, F., and Timme, S., "Delayed Detached–Eddy Simulation of Shock Buffet on Half Wing–Body Configuration," *AIAA Journal*, Vol. 55, No. 4, 2017, pp. 1230–1240.

[36] Timme, S., "Global Shock Buffet Instability on NASA Common Research Model," 2019. AIAA 2019-0037.

[37] Masini, L., Timme, S., and Peace, A. J., "Scale-Resolving Simulation of Shock Buffet Onset Physics on a Civil Aircraft Wing," *Royal Aeronautical Society 2018 Applied Aerodynamics Conference*, 2018.

[38] Masini, L., Timme, S., Ciarella, A., and Peace, A. J., "Influence of Vane Vortex Generators on Transonic Wing Buffet: Further Analysis of the BUCOLIC Experimental Dataset," *52nd 3AF International Conference on Applied Aerodynamics*, 2017. FP14-AERO2017-masini.

[39] Masini, L., Timme, S., and Peace, A. J., "Analysis of a Civil Aircraft Wing Transonic Shock Buffet Experiment," 2019. Manuscript under review.

[40] Taira, K., Brunton, S. L., Dawson, S. T. M., Rowley, C. W., Colonius, T., McKeon, B. J., Schmidt, O. T., Stanislav, S., Theofilis, V., and Ukeiley, L. S., "Modal Analysis of Fluid Flows: An Overview," *AIAA Journal*, Vol. 55, No. 12, 2017, pp. 4013–4041.

[41] Ohmichi, Y., Ishida, T., and Hashimoto, A., "Modal Decomposition Analysis of Three-Dimensional Transonic Buffet Phenomenon on a Swept Wing," *AIAA Journal*, Vol. 56, No. 10, 2018, pp. 3938–3950.

[42] Sartor, F., and Timme, S., "Reynolds-Averaged Navier-Stokes Simulations of Shock Buffet on Half Wing-Body Configuration," 2015. AIAA 2015-1939.

[43] Timme, S., and Thormann, R., "Towards Three-Dimensional Global Stability Analysis of Transonic Shock Buffet," 2016. AIAA 2016-3848.

[44] "U.S. Standard Atmosphere, 1976," Tech. Rep. NASA-TM-X-74335, NASA, 1976.

[45] Allmaras, S. R., Johnson, F. T., and Spalart, P. R., "Modifications and Clarifications of the Spalart-Allmaras Turbulence Model," 2012. ICCFD7-1902.

[46] Probst, A., and Reuß, S., "Scale-Resolving Simulations of Wall-Bounded Flows with an Unstructured Compressible Flow Solver," *Progress in Hybrid RANS-LES Modelling*, Vol. 130, 2015, pp. 481–491.

[47] Crouch, J., Garbaruk, A., and Magidov, D., "Predicting the Onset of Flow Unsteadiness Based on Global Instability," *Journal of Computational Physics*, Vol. 224, No. 2, 2007, pp. 924–940.

[48] Spalart, P. R., Strelets, W.-H., and Allmaras, S. R., "Comments on the feasibility of LES for wings, and on a hybrid RANS/LES approach," *Proceedings of first AFOSR international conference on DNS/LES*, 1997.

[49] Spalart, P. R., Deck, S., Shur, M. L., Squires, K. D., Strelets, M. K., and Travin, A., "A New Version of Detached-Eddy Simulation, Resistant to Ambiguous Grid Densities," *Theoretical and Computational Fluid Dynamics*, Vol. 20, No. 3, 2006, pp. 181–195.

[50] Spalart, P. R., "Detached-eddy Simulation," *Annual review of fluid mechanics*, Vol. 41, 2009, pp. 181–202.

[51] Probst, A., and Reuß, S., "Progress in Scale-Resolving Simulations with the DLR-TAU Code," Tech. Rep. 420051, DLR, 2016.

[52] Löwe, J., Probst, A., Knopp, R., and Jarrin, N., "A Low-Dissipation Low-Dispersion Second-Order Scheme for Unstructured Finite-Volume Flow Solvers," 2015. AIAA 2015-0815.

[53] Probst, A., Löwe, J., Reuß, S., and Kessler, R., "Scale-Resolving Simulations with a Low-Dissipation Low-Dispersion Second-Order Scheme for Unstructured Finite-Volume Flow Solvers," 2015. AIAA 2015-0816.

[54] Spalart, P. R., and Streett, C., "Young-Person's Guide to Detached-Eddy Simulation Grids," Tech. Rep. CR-2001-211032, NASA, 2001.

[55] Shaw, J. A., Stokes, S., and Lucking, M. A., "The Rapid and Robust Generation of Efficient Hybrid Grids for RANS Simulations over Complete Aircraft," *International Journal for Numerical Methods in Fluids*, Vol. 43, No. 6-7, 2003, pp. 785–821.

[56] Rudnik, R., Melber-Wilkending, S., and Risley-Settle, P., "TAU-SOLAR Contributions to the 3rd High Lift Prediction Workshop," 2018. AIAA 2018-1035.

[57] Sirovich, L., "Turbulence and the Dynamics of Coherent Structures. I. Coherent Structures," *Quarterly of Applied Mathematics*, Vol. 45, No. 3, 1987, pp. 561–571.

[58] Belson, B. A., Tu, J. H., and Rowley, C. W., "Algorithm 945: Modred—a Parallelized Model Reduction Library," *ACM Transactions on Mathematical Software*, Vol. 40, No. 4, 2014, pp. 1–23.

[59] Sartor, F., and Timme, S., "Mach Number Effects on Buffeting Flow on a Half Wing-Body Configuration," *International Journal of Heat and Fluid Flow*, Vol. 26, No. 7, 2016, pp. 2066–2080.

[60] Burg, J. P., "Maximum Entropy Spectral Analysis," *37th Annual International Meeting of the Society of Exploration Geophysicists*, 1967.

[61] Wilcox, D. C., *Turbulence Modeling for CFD*, DCW Industries, Inc, La Cãnada, CA, 1993.

[62] Welch, P., "The Use of Fast Fourier Transform for the Estimation of Power Spectra: A Method Based on Time Averaging over Short, Modified Periodograms," *IEEE Transaction on Audio and Electroacoustics*, Vol. 15, No. 2, 1967, pp. 70–73.

[63] Tu, J. H., Rowley, C. W., Luchtenburg, D. M., Brunton, S. L., and Kutz, J. N., "On Dynamic Mode Decomposition: Theory and Applications," *Journal of Computational Dynamics*, Vol. 1, No. 2, 2014, pp. 391–421.